Introduction

Correlation between arterial carbon dioxide tension and cerebral blood flow is well established [Kety & Schmidt 1948, Shimosegawa et al. 1995, Kuwabara et al. 1997]. However, responsiveness of myocardial blood flow to hypercapnea and hypocapnea has not been fully elucidated. These relationships were investigated in animal experiments [Feinberg et al. 1960, Love et al. 1965, Case & Greenberg 1976, Bos et al. 1979, Powers et al. 1986] and human clinical studies [Rowe et al. 1962, Neill & Hattenhauer 1975, Wilson et al. 1981, Kazmaier et al. 1998] with conflicting results. The inconsistencies observed should be attributable to differences in experimental conditions, such as the techniques used for measurement, or whether the studies were performed in animals or humans, or presence versus absence of ischemic heart disease.

In this study, we evaluated the responses of myocardial blood flow and cerebral blood flow to hypercapnea and hypocapnea in healthy elderly men. We employed a dual positron emission tomography (PET) scanner consisting of two scanners to measure myocardial blood flow and cerebral blood flow simultaneously in the same subject [Iida et al. 1998]. PET allows assessment of functional parameters under physiological conditions. Using this dual PET scan technique allowed simultaneous assessment of myocardial and cerebral circulations, noninvasively and reliably and enabled comparison of the two.

Materials and Methods

Study Subjects

Thirteen healthy men (age range 51-71 years; mean 59.4, standard deviation [5.5]) who had been the subjects of previously published studies with different objectives [Iida et al. 1998, Ito et al. 1999, Ito et al. 2000, Ito et al. 2002] took part in the study. These men had normal laboratory parameters, no signs or symptoms of ischemia in the heart or brain, and no abnormalities were found by brain magnetic resonance imaging, electrocardiography, cardiac echocardiography, and physical examination. All subjects provided written informed consent that data obtained from the PET studies could be used for research purposes. The study protocol was approved by the Ethics Committee of the Research Institute of Brain and Blood Vessels, Akita, Japan.

PET Procedures

The Headtome V dual PET system (Shimadzu Corp., Kyoto, Japan), a combination of the two Headtome V PET scanners, was used for all studies [Iida et al. 1998]. The system allowed simultaneous imaging of the brain and heart and provided 47 sections for the brain and 31 sections for the heart with center-to-center distances of 3.125 mm. The intrinsic spatial resolution was 4.0 mm in-plane and 4.3 mm full-width at half-maximum axially. All PET data were acquired in 2D mode and reconstructed with a Butterworth filter, resulting in a final in-plane resolution of approximately 8 mm full-width at half-maximum.

After an overnight fast, subjects were placed in the supine position on the scanner bed. The blood-pool images were obtained 1 minute after continuous inhalation of ^{15}O-CO gas (approximately 5 GBq total applied to the mouth). One minute after the end of ^{15}O-CO gas inhalation, ^{15}O-CO blood-pool images of the heart were obtained with an R-wave triggered electrocardiogram gated tomographic scan. A simultaneous gated static scan on both the heart and brain was done 4 minutes after the inhalation of ^{15}O-CO gas. Three venous blood samples were taken during the ^{15}O-CO scan, and the radioactivity concentration in the whole blood was measured using a NaI-well counter that was cross-calibrated with the PET scanner. ^{15}O-CO blood-pool images were used to draw regions of interests on left ventricular cavity and left ventricular wall accurately to obtain time activity curves. The recovery of

4

coefficient of left ventricular cavity was given by the myocardial static blood volume image and was also used to determine myocardial blood flow [Iida et al. 1998]. After 12-15 minutes, to allow for decay of ^{15}O-radioactivity to background levels, transmission scanning was undertaken over 10 minutes. Then, $H_2^{15}O$ PET studies were performed at rest, and under hypercapnea and hypocapnea. The order of the studies was rest, hypercapnea, and hypocapnea studies in 7 subjects, and rest, hypocapnea, and hypercapnea studies in 6 subjects. The intervals between $H_2^{15}O$ PET studies were at least 15 minutes to allow the decay of radioactivity. Following the continuous intravenous infusion of $H_2^{15}O$ (1.1-1.4 GBq) over 2 minutes, 180-sec static imaging of the brain and 360-sec dynamic imaging of the heart were commenced. The dynamic data of the heart consisted of twelve 5- seconds frames, eight 15-seconds frames, and six 30- seconds frames. Hypercapnea was achieved by inhalation of 7% CO_2 gas, beginning 1 minute before ^{15}O-water injection and continuing until the end of the imaging of the heart. Hypocapnea was induced by hyperventilation. Three arterial blood samples were taken during each PET scan to measure arterial carbon dioxide tension and pH.

Data Analysis

Cerebral blood flow images were generated from the PET data as described previously [Iida et al. 1998], and a region of interest for the inside of the brain contour was drawn on a slice of the cerebral blood flow image that was at the level of the basal ganglia. The region of interest was determined on an image obtained at rest and applied to images obtained under stress conditions. The mean cerebral blood flow in the region of interest was calculated from ^{15}O-H_2O autoradiography method [Raichle ME et al. 1983] and used for the following analyses. The percent change in cerebral blood flow at hypercapnea was defined as 100 × (cerebral blood flow at hypercapnea - cerebral blood flow at rest) / cerebral blood flow at rest, and cerebral blood flow responsiveness to hypercapnea was calculated as percent change in cerebral blood flow at hypercapnea divided by arterial carbon dioxide tension at hypercapnea minus arterial carbon dioxide tension at rest. The percent change in cerebral blood flow at hypocapnea and cerebral blood flow responsiveness to hypocapnea were determined using similar calculations, but using hypocapnea values instead.

The region of interests for the left ventricular cavity and the whole anterolateral wall

of the left ventricle at mid ventricular level were drawn on a slice of the short-axis myocardial images. The region of interests for the image at rest were copied on the myocardial images under the stress conditions. The myocardial blood flow value was estimated using the regions of interests according to a previously validated method [Iida et al. 1998]. In summary, myocardial blood flow was calculated using a non-linear least squares fitting technique of the left ventricular tissue and arterial $^{15}O-H_2O$ time activity curves [Iida H et al. 1988]. The input function was non-invasively determined from the time activity curve of left ventricular cavity [Iida H et al. 1992]. Time activity curve of the left ventricular cavity and that of the myocardial wall were fitted to the previously demonstrated tracer kinetic model equations to determine myocardial blood flow [Iida et al. 1998]. The percent change in myocardial blood flow at hypercapnea was defined as $100 \times$ (myocardial blood flow during hypercapnea - myocardial blood flow at rest) / myocardial blood flow at rest, and myocardial blood flow responsiveness to hypercapnea was calculated as percent change in myocardial blood flow during hypercapnea divided by arterial carbon dioxide tension under hypercapnea minus arterial carbon dioxide tension at rest. The percent change in myocardial blood flow during hypocapnea and myocardial blood flow responsiveness to hypocapnea were determined using similar calculations but using hypocapnea values instead. In addition, normalized myocardial blood flow was calculated for the rate pressure product by the equation:

Normalized myocardial blood flow = $10000 \times$ myocardial blood flow / rate pressure product, and percent change in normalized myocardial blood flow and normalized myocardial blood flow responsiveness were calculated.

Statistical Analysis

Values were expressed as the mean ± standard deviation. Comparisons were made by one-way analysis of variance followed by Fisher's least significant difference tests for parametric distributions and Kruskal-Wallis test followed by Scheffe's test for nonparametric distributions. A P value < 0.05 was considered statistically significant.

Results

Hemodynamics

Blood pressures, heart rate, rate pressure product, arterial carbon dioxide tension and pH are summarized in Table 1. Blood pressures were measured in the thigh because arteries and veins in both arms were cannulated. Since the blood pressure measured in the thighs were on average 25 mmHg higher than those measured in the arms in our institution, blood pressures in the thigh were considered to be within normal range. Electrocardiogram findings under hypercapnea or hypocapnea did not change compared with those at rest. Arterial carbon dioxide tension significantly decreased during hypocapnea and significantly increased during hypercapnea. Blood pressures significantly increased during hypercapnea but remained unchanged during hypocapnea. Rate pressure product did not change significantly during hypocapnea but significantly increased during hypercapnea.

Cerebral blood flow

Cerebral blood flow significantly decreased during hypocapnea and significantly increased during hypercapnea (Table2). The change in cerebral blood flow caused by hypocapnea was -32.2 percent ± 11.3 percent, and the cerebral blood flow responsiveness to hypocapnea was 3.0 ± 1.1 percent /mmHg. The change in cerebral blood flow caused by hypercapnea was 21.0 percent ± 15.5 percent, and the cerebral blood flow responsiveness to hypercapnea was 8.2 ± 5.3 percent /mmHg.

Myocardial blood flow

Hypocapnea caused a significant reduction in myocardial blood flow from baseline (Table 2). The percent change in myocardial blood flow caused by hypocapnea was -29.3 percent ± 15.1 percent, and the myocardial blood flow responsiveness to hypocapnea was 3.5 ± 3.0 percent /mmHg. Normalization for rate pressure product did not alter the percent change (- 30.4 percent ± 16.5 percent) and responsiveness (-2.2 ± 11.2 percent /mmHg) substantially. Under hypocapnea, the percent changes in cerebral blood flow, myocardial blood flow, and normalized myocardial blood flow were not significantly different compared with baseline. There were no significant differences in the responsiveness to hypocapnea between cerebral blood flow, myocardial blood flow, and normalized myocardial blood flow.

Hypercapnea significantly increased myocardial blood flow. The percent change in myocardial blood flow caused by hypercapnea was 12.5 percent ± 15.6 percent, and the myocardial blood flow responsiveness to hypercapnea was 5.2 ± 9.9 percent /mmHg. However, the increase in myocardial blood flow disappeared after normalization for rate pressure product. The change in normalized myocardial blood flow under hypercapnea was -2.2 percent ± 11.2 percent, and the normalized myocardial blood flow responsiveness to hypercapnea was -1.7 ± 8.8 percent /mmHg. As for hypercapnea, the percent change in normalized myocardial blood flow was significantly smaller than the change in cerebral blood flow ($p < 0.05$), and the normalized myocardial blood flow responsiveness was significantly smaller than cerebral blood flow responsiveness ($p < 0.05$).

Discussion

We simultaneously measured myocardial blood flow and cerebral blood flow at rest, during hypocapnea, and during hypercapnea in healthy elderly men. During hypocapnea, cerebral blood flow was reduced significantly as expected, and myocardial blood flow also diminished significantly to a similar magnitude. Rate pressure product did not change significantly from baseline, and myocardial blood flow normalized for rate pressure product also decreased. These results indicate that hypocapnea depresses myocardial blood flow, independently of cardiac workload, in healthy elderly men. The responsiveness to hypocapnea was similar between cerebral blood flow and myocardial blood flow, suggesting that hypocapnea can induce vasoconstriction in both heart and brain in healthy elderly men.

Several studies of coronary vascular response to hypocapnea using experimental animals have been reported however, the results were inconsistent [Feinberg 1960, Love 1965, Case 1976]. In a study of humans **with** negligible coronary artery disease, hypocapnea with 30.6 percent reduction in arterial carbon dioxide tension resulted in a significant 30.3 percent reduction in myocardial blood flow with a wide range of variability [Rowe 1962]. The present results are consistent with these previous studies. However, in studies of patients with coronary artery disease, hypocapnea resulted in a mild but significant 12 percent reduction in myocardial blood flow [Neill & Hattenhauer 1975] or did not change significantly [Wilson et al. 1981, Kazmaier et al. 1998]. Therefore, myocardial blood flow response to hypocapnea is likely to be different between normal subjects and patients with coronary artery disease. Since myocardial blood flow response to hypocapnea did not differentiate regions with myocardial ischemia from regions of non-ischemic myocardium in these studies of coronary artery disease, further study is required to clarify whether myocardial blood flow response to hypocapnea would differ between ischemic myocardium and non-ischemic myocardium.

Myocardial blood flow response to hypercapnea remains controversial. A number of experimental animal studies showed that hypercapnea did not increase myocardial blood flow [Feinberg et al. 1960, Love et al. 1965, van den Bos et al. 1979], whereas other studies showed that hypercapnea could increase myocardial blood flow [Case & Greenberg 1975, Powers et al. 1986]. In a study of anesthetized patients with coronary artery disease before

9

surgery, elevation of arterial carbon dioxide tension (+10 mmHg) resulted in a 15 percent increase in myocardial blood flow [Kazmaier et al. 1998]. However, the study did not estimate normalized myocardial blood flow to exclude the influence of cardiac workload on myocardial blood flow measurement [Kazmaier et al. 1998]. In this study, hypercapnea significantly increased myocardial blood flow and cerebral blood flow but not normalized myocardial blood flow with rate pressure product in healthy elderly men. Myocardial blood flow responsiveness to hypercapnea was significantly lower than that in cerebral blood flow when myocardial blood flow was normalized with respect to rate pressure product. Increase in cardiac workload under hypercapnea could explain an increase in myocardial blood flow. However, hypercapnea did not have an additional direct effect to increase myocardial blood flow independent of an elevation in cardiac workload under mild hypercapnea. Since myocardial blood flow responsiveness to hypercapnea was significantly lower than that in cerebral blood flow when myocardial blood flow was normalized with respect to cardiac workload, vascular responsiveness to hypercapnea is expected to be different between heart and brain. In this study, the magnitude of increase in arterial carbon dioxide tension during hypercapnea was small (3 mmHg), contrasting with the magnitude of decrease in arterial carbon dioxide tension during hypocapnea (11 mmHg). Such difference in the magnitude of changes in arterial carbon dioxide tension may explain why hypocapnea was effective to decrease the normalized myocardial blood flow but hypercapnea had no effect to increase the normalized myocardial blood flow. However, even under such very small increase in carbon dioxide tension, significantly elevated myocardial blood flow without normalization in response to an increase in cardiac workload was seen. Therefore, the importance of the carbon dioxide tension changes in determining the response of heart and brain perfusion could be discussed more than is presently done. To resolve such issues, much stronger hypercapneic stress test at different hypercapnic levels to increase arterial carbon dioxide tension is required to clarify whether hypercapnea directly increases myocardial blood flow independent of an increase in cardiac workload. Use of beta-blockers to exclude an influence of increase in cardiac workload for the myocardial blood flow measurement during hypercapnea [van den Bos et al. 1979, Powers et al. 1986] would also be helpful to understand myocardial blood

10

flow responsiveness to hypercapnea. For future studies, it is of interest to test the effect of normalization with both cardiac workload and arterial carbon dioxide tension changes on the studies of myocardial blood flow.

Conclusion

In normal elderly men, hypocapnea produces similar vasoconstriction in both heart and brain. Mild hpercapnea increased cerebral blood flow but did not have an additional effect to dilate coronary arteries beyond the expected range in response to an increase in cardiac workload.

Conflict of interest

No conflict of interest exists in connection with this article.

References

Case, RB. & Greenberg, H. 1976. The response of canine coronary vascular resistance to local alterations in coronary arterial P CO2. *Circ Res* **39**, 558-66.

Feinberg, H., Gerola, A. & Katz, LN. 1960. Effect of changes in blood CO2 level on coronary flow and myocardial O2 consumption. *Am J Physiol* **199**, 349-354.

Iida, H., Kanno, I., Takahashi, A., Miura, S., Murakami, M., Takahashi, K., Ono, Y., Shishido, F., Inugami, A., Tamura, N., & Tomura, N. 1988. Measurement of absolute myocardial blood flow with H215O and dynamic positron-emission tomography. Strategy for quantification in relation to the partial-volume effect. *Circulation* **78**,104-115.

Iida, H., Miura, S., Shoji, Y., Ogawa, T., Kado, H., Narita, Y., Hatazawa, J., Eberl, S., Kanno, I. & Uemura, K. 1998. Non-invasive quantitation of CBF using oxygen-15-water and a dual-PET system. *J Nucl Med* **39**, 1789-1798.

Iida, H., Rhodes, CG., de Silva, R., Araujo, LI., Bloomfield, PM., Lammertsma, AA., & Jones, T. 1992. Use of the left ventricular time-activity curve as a noninvasive input function in dynamic oxygen-15-water positron emission tomography. J Nucl Med **33**,1669-1677.

Ito, H., Kinoshita, T., Tamura, Y., Yokoyama, I. & Iida, H. 2000. Effect of intravenous dipyridamole on cerebral blood flow in humans. A PET Study. *Stroke* **30**, 1616-1620.

Ito, H., Yokoyama, I., Iida, H., Kinoshita, T., Hatazawa, J., Shimosegawa, E., Okudera, T. & Kanno, I. 2000. Regional differences in cerebral vascular response to PaCO2 changes in humans measured by PET. *J Cerebral Blood Flow and Metab* **20**, 1264-1270.

Ito, H., Yokoyama, I., Tamura, Y., Kinoshita, T., Hatazawa, J., Kawashima, R. & Iida, H. 2002. Regional changes in human cerebral blood flow during dipyridamole stress: Neural activation in the thalamus and prefrontal cortex. Neuroimage **16**, 788-793.

Kazmaier, S., Weyland, A., Buhre, W., Stephan, H., Rieke, H., Filoda, K. & Sonntag, H. Effects of respiratory alkalosis and acidosis on myocardial blood flow and metabolism in patients with coronary artery disease. *Anesthesiology* **89**, 831-837.

Kety, SS. & Schmidt, CF. 1948. The effects of altered arterial tensions of carbon dioxide and oxygen on cerebral blood flow and cerebral oxygen consumption of normal young men. *J Clin Invest* **27**, 484-492.

Kuwabara, Y., Ichiya, Y., Sasaki, M., Yoshida, T., Masuda, K., Matsushima, T. & Fukui, M. 1997. Response to hypercapnia in moyamoya disease. Cerebrovascular response to hypercapnia in pediatric and adult patients with moyamoya disease. *Stroke* **28**, 701-707.

Love, WD., Tyler, MD., Abraham, RE. & Munford, RS. 1965. Effects of O2, CO2, and drugs on estimating coronary blood flow from Rb86 clearance. *Am J Physiol* **208**, 1206-1210.

Neill, WA. & Hattenhauer, M. 1975. Impairment of myocardial O2 supply due to hyperventilation. *Circulation* **52**, 854-858.

Powers, ER., Bannerman, KS., Fitz-James, I., & Cannon, PJ. 1986. Effect of elevations of coronary artery partial pressure of carbon dioxide (PCO2) on coronary blood flow. *J Am Coll Cardiol* **8**, 1175-1181.

Raichle, ME., Martin, WRW., Herscovitch, P., Mintun, MA., & Markham, J. 1983. Brain blood flow measured with intravenous H2(15)O. II. Implementation and validation. *J Nucl Med* **24**, 790-798.

Rowe, GG., Castillo, CA. & Crumpton, CW. 1962. Effects of hyperventilation on systemic and coronary hemodynamics. *Am Heart J* **63**, 67-77.

Shimosegawa, E., Kanno, I., Hatazawa, J., Fujita, H., Iida, H., Miura, S., Murakami, M., Inugami, A., Ogawa, T., Itoh, H., Okudera, T. & Umemura, K. 1995. Photic stimulation study of changing the arterial partial pressure level of carbon dioxide. *J Cereb Blood Flow Metab* **15**, 111-114.

van den Bos, GC., Drake, AJ. & Noble, MI. 1979. The effect of carbon dioxide upon myocardial contractile performance, blood flow and oxygen consumption. *J Physiol* **287**, 149–162.

Wilson, JR., Goldberg, S., Hirshfeld, JW. & Harken, AH. 1981. Effects of respiratory alkalosis on coronary vascular dynamics and myocardial energetics in patients with coronary artery disease. *Am Heart J* **102**, 202-205.

Table 1. Hemodynamics, arterial carbon dioxide tension and pH during $H_2{}^{15}O$ PET studies

	Rest	Hypercapnea	Hypocapnea
Systolic blood pressure (mmHg)	146.5 ±20.9	159.8 ±25.4	144.8 ±26.7
Diastolic blood pressure (mmHg)	82.8 ±12.0	85.3 ±10.7	78.5 ±13.2
Heart rate (beat / minute)	58.4 ±7.8	61.6 ±8.7	60.7 ±7.8
Rate pressure product	8472 ±1146	9758 ±1609	8717 ±1677
Arterial carbon dioxide tension	40.2 ±2.4	43.1 ±2.7* $	29.2 ±3.4† $
pH	7.417 ±0.013	7.385 ±0.019 $	7.505 ±0.039 $

Data are presented as mean ± standard deviation.

Significance of changes compared with the three groups: *$P<0.05$, †$P<0.01$ by Fisher PLSD,

Significance of changes compared with the resting condition: $P<0.05$, $ $P < 0.01$ by Wilcoxon signed rank test

Table 2. Cerebral blood flow (mL•minute^{-1}•[100 gram of perfusable tissue]$^{-1}$), myocardial blood flow (mL•minute^{-1}•[100 gram of perfusable tissue]$^{-1}$), and normalized myocardial blood flow (100mL•mmHg^{-1}•[heart-beat]$^{-1}$•[gram of perfusable tissue]$^{-1}$)

	Rest	Hypocapnea	Hypercapnea
Cerebral blood flow	39.8 ±5.3	27.0 ±6.3†	48.4 ±10.4*
Myocardial blood flow	78.2 ±12.6	55.1 ±14.6†	88.7 ±22.4
Normalized myocardial blood flow	93.4 ±16.6	64.5 ±18.3†	90.5 ±14.3

Significance of changes compared with the three groups: *$P < 0.05$, †$P < 0.01$

NOTE

Acceleration of Monte Carlo-based scatter compensation for cardiac SPECT

A Sohlberg[1,2], H Watabe[1] and H Iida[1]

[1] National Cardiovascular Center Research Institute, 5-7-1 Fujishiro-dai, Suita City, 565-8565 Osaka, Japan
[2] HERMES Medical Solutions, Skeppsbron 44, 111 30 Stockholm, Sweden

E-mail: antti.sohlberg@hermesmedical.com

Abstract

Single proton emission computed tomography (SPECT) images are degraded by photon scatter making scatter compensation essential for accurate reconstruction. Reconstruction-based scatter compensation with Monte Carlo (MC) modelling of scatter shows promise for accurate scatter correction, but it is normally hampered by long computation times. The aim of this work was to accelerate the MC-based scatter compensation using coarse grid and intermittent scatter modelling. The acceleration methods were compared to un-accelerated implementation using MC-simulated projection data of the mathematical cardiac torso (MCAT) phantom modelling ^{99m}Tc uptake and clinical myocardial perfusion studies. The results showed that when combined the acceleration methods reduced the reconstruction time for 10 ordered subset expectation maximization (OS-EM) iterations from 56 to 11 min without a significant reduction in image quality indicating that the coarse grid and intermittent scatter modelling are suitable for MC-based scatter compensation in cardiac SPECT.

1. Introduction

The quality of single proton emission computed tomography (SPECT) is degraded by attenuation, collimator blurring and scatter. Whereas attenuation and collimator blurring can nowadays be corrected in clinically acceptable times, accurate and efficient scatter correction has been proven to be a more difficult problem. This is mainly due to the fact that the shape of the scatter point-spread function depends on the location inside the object and can be very difficult to parametrize.

One very promising recently presented scatter compensation method is the Monte Carlo (MC)-based scatter correction by Beekman *et al* (2002). In this method, a MC simulator is used as a forward-projector for scatter in the ordered subset expectation maximization

N277

(OS-EM) algorithm (Hudson and Larkin 1994). MC-based scatter modelling is expected to be especially advantageous in areas where the attenuating media is highly non-uniform such as the thorax, because it can faithfully produce the complex shape of the scatter response function. The MC-based scatter compensation has been shown to outperform the common triple-energy window scatter compensation method in terms of contrast and myocardial lesion detectability (Xiao *et al* 2006). Unfortunately, despite the considerable advances made in MC-based scatter compensation its widespread utilization in clinical practice can still be limited by long computation times.

Kadrmas *et al* (1998) have presented two simple and effective acceleration methods for reconstruction-based scatter compensation. The first of these approaches is the coarse grid scatter modelling method, which calculates the scatter contribution using sparser grid than is used in the actual reconstruction. The second approach is the intermittent scatter modelling method, where scatter is modelled only during the first couple of OS-EM iterations and then held as a constant additive factor for the later iterations. Both of these approaches are based on the assumption that the scatter response contains mainly low-frequency components and can thus be modelled with a relatively large voxel size and not during the last OS-EM iterations. Kadrmas *et al* presented their acceleration methods for the effective scatter source estimation method (Frey and Tsui 1996) and showed that the performance of the accelerated scatter compensation was very similar to the performance of the standard (un-accelerated) scatter correction.

The goal of this work was to implement the coarse grid and intermittent scatter modelling methods for MC-based scatter compensation and to evaluate their performance in case of ^{99m}Tc cardiac SPECT.

2. Materials and methods

2.1. Implementation of the MC simulator

MC simulations are based on sampling radioactive decays within a source volume and following their interactions inside the attenuating media. Our MC simulator uses four different maps in the simulations: emission map for setting photons to be tracked, density map for sampling interactions and primary and scatter maps for storing photon weights. The history of each photon (primary or scatter) in our simple MC simulator is tracked shortly as follows:

(1) If the simulated photon is a primary the primary map is updated. Otherwise direction cosines are sampled and random walk is started for the scatter photon.

(2) Photon interaction points are calculated using the delta scattering algorithm (Woodcock *et al* 1965), which does not require ray tracing through the attenuating media. The basic principle of delta scattering is that the path-length P between two 'fictious' interaction points is sampled as $P = -\ln(R)/\mu_{max}$, where R is a uniform random number and μ_{max} is the largest attenuation coefficient in the attenuating media (Ljungberg *et al* 2005). At the end of the sampled path a possible interaction is sampled according to established methods or tracking is continued by sampling a new distance P according to the above-mentioned equation.

(3) At each real interaction point photon weight is multiplied by the probability that no photoelectric effect occurred and a copy of the original photon is forced to Compton scatter towards the detector and scatter map is updated according to the convolution-based forced detection approach (de Jong *et al* 2001).

(4) If predetermined number of scattering events has not been reached, the history of the
original photon is continued by Compton scatter. New direction cosines are sampled
from the Klein–Nishina function and tracking is continued from (2).

After all the photons have been simulated the primary and scatter maps are multiplied by
probability that photon emitted from a certain voxel reaches the detector without interaction.
Then these maps are convolved with depth-dependent detector response function, which is
assumed to be Gaussian. The blurred primary and scatter maps are finally forward-projected
to primary and scatter projections.

2.2. Implementation of the reconstruction algorithm with MC-based scatter compensation

The developed MC simulator was included into an OS-EM reconstruction algorithm as
forward-projector for the scattered counts as originally proposed by Beekman *et al* (2002).
The OS-EM is given by

$$f_j^{new} = \frac{f_j^{old}}{\sum_{i \in S_n} a_{ij}} \sum_{i \in S_n} a_{ij} \frac{p_i}{\sum_k a_{ik} f_k^{old} + s_i},$$ (1)

where f is the reconstructed image, p is the measured projections, j (or k) is the reconstruction
voxel index, i is the projection pixel index, a_{ij} is the probability that emission from voxel j
is detected in pixel i, s is the MC-based scatter projections and S_n is the nth subset. The
image update in OS-EM consists of sequential forward- and back-projection operations.
The estimated projections are obtained by forward-projecting the current image estimate
$\left(\sum_k a_{ik} f_k^{old}\right)$, and correction terms that are used to update the old image are formed by back-
projecting the ratio of the measured and estimated + scatter projections $\left(\sum_{i \in S_n} a_{ij} \frac{p_i}{\sum_k a_{ik} f_k^{old} + s_i}\right)$.

In this work the forward- and back-projectors were implemented as rotation based
(Di Bella *et al* 1996). The back-projector included attenuation and detector response
compensation and the forward-projector attenuation, detector response and MC-based scatter
compensation. Attenuation correction factors for each voxel were calculated simply by
summing the rotated attenuation map along columns. Detector response, on the other hand,
was modelled by convolving each plane of the reconstruction matrix parallel to the projection
plane with collimator response kernel, which was assumed to be Gaussian. The scatter
projection for each projection angle was obtained by MC-based forward-projection of the
current image estimate.

2.3. Acceleration of MC-based scatter compensation

The coarse grid scatter modelling method was implemented by simply down-sampling the
current image estimate (and the attenuation map) into a sparser matrix before the MC-based
forward-projection and linearly interpolating the scatter projections back to the original size
after forward-projection was finished. In the intermittent acceleration approach the MC-based
scatter modelling is performed only in the few early OS-EM iterations and after that the scatter
projections are kept fixed for remaining iterations.

2.4. Performance tests

Performance tests were performed using a female version of the mathematical cardiac torso
(MCAT) phantom (Tsui *et al* 1994), and the camera parameters are shown in table 1.
The MCAT phantom modelled normal human tissue densities in the thorax region and
the source distribution presented the ^{99m}Tc uptake with the following relative activities per
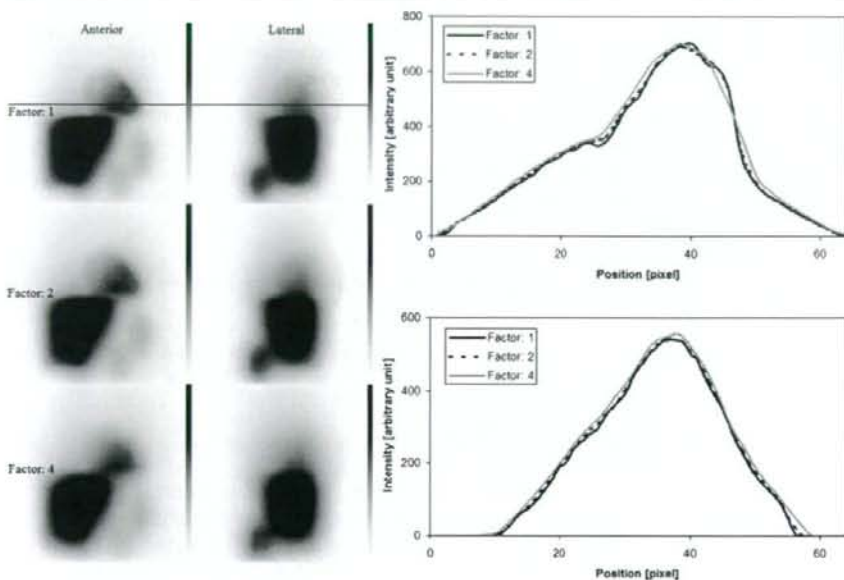
Figure 1. Comparison of scatter projections and profiles obtained with different down-sampling factors (factor: 1 is scatter projection without down-sampling). Upper profile is obtained from the anterior projection and lower from the lateral projection. Locations of the profiles are shown as horizontal lines.

Table 1. Camera parameters for Monte Carlo simulations.

Low-energy high-resolution collimator (4.0 cm hole length, 0.178 cm hole diameter)
0.4 cm intrinsic detector resolution
9.0% energy resolution
15.0% energy window centred on 140 keV
23.0 cm radius of rotation

voxel: myocardium 100, liver 50, kidney 100, spleen 80, lung 5 and rest of the body 2.5. Two lesions (anterior and inferior) with the relative uptake of 2.5 were included in the left myocardium.

The effects of different down-sampling factors in the coarse grid scatter modelling scheme were studied by performing MC simulations using the MCAT phantom. The pixel size was set to 0.625 cm (64×64 projection and $64 \times 64 \times 64$ image matrix size). Down-sampling factors of 2 ($64 \times 64 \times 64$ image matrix down-sampled to $32 \times 32 \times 32$ matrix) and 4 ($64 \times 64 \times 64$ image matrix down-sampled to $16 \times 16 \times 16$ matrix size) were investigated. Figure 1 presents anterior and lateral scatter projection images of the MCAT phantom. According to this figure factor 4 produces slightly distorted scatter projections, and thus the down-sampling factor was set to 2 for all the reconstructions accelerated with the coarse grid scatter modelling.

The effect of the number of scatter update iterations was studied by using MCAT projection data simulated using the SIMIND MC simulator (Ljungberg and Strand 1989). The camera parameters for this simulation are again shown in table 1. The number of simulated noise-free
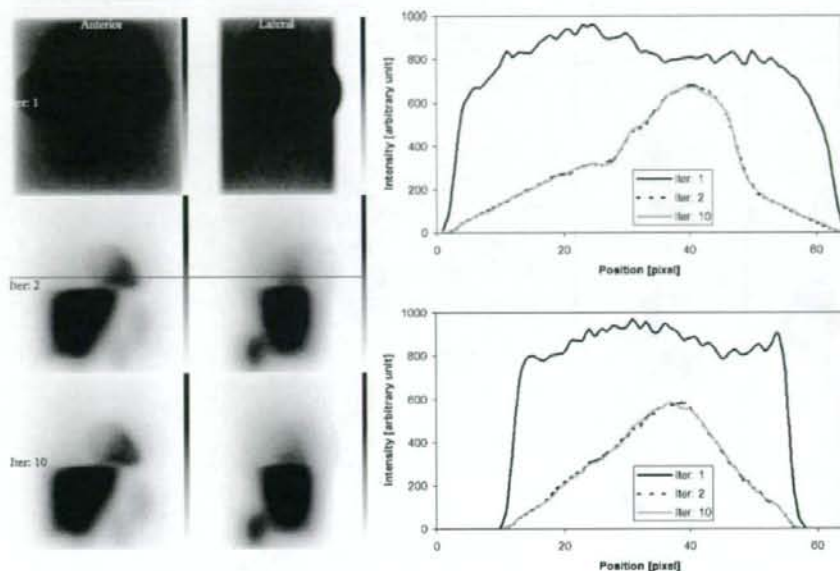
Figure 2. Comparison of different number of scatter update iterations. Upper profile is obtained from the anterior projection and lower from the lateral projection. Locations of the profiles are shown as horizontal lines.

projections was 64 on a 360° orbit and pixel size was 0.3125 cm (128 × 128 projection and 128 × 128 × 128 image matrix size). The projections were collapsed to a 64 × 64 matrix size before the reconstruction. Reconstruction using the noise-free projection data was performed with 16 subsets and 1–10 iterations, and the MC forward-projected scatter projections were saved after every iteration. Figure 2 presents scatter projection images and profiles for different iteration numbers, and these images show that the scatter projections do not change markedly after two iterations. Therefore, in the following performance tests only two scatter iterations were used when intermittent scatter modelling was applied.

The acceleration methods were tested using the same MCAT projection data that were used to find the scatter iterations stopping point. Poisson noise was added to the noise-free projections by setting number of total counts to 5 million. The projections were reconstructed without scatter compensation, with the MC-based scatter compensation but without acceleration, with coarse grid scatter modelling (down-sampling factor of 2), with intermittent scatter modelling (scatter updated during the first two iterations) and with both accelerations applied at the same time. Number of MC simulated photons per projection angle was set to 1.0 million and 16 subsets with 10 iterations were used. After reconstruction images were filtered with a 3D Butterworth filter (order: 5, cutoff: 1.0 cm^{-1}), transverse slices were zoomed and reoriented into short-axis slices. Regions of interest (ROI) were drawn on the normal myocardium, ventricle and on the anterior/inferior defect areas. Normal myocardium to ventricle and normal myocardium to lesion contrasts were calculated.

In addition to Monte Carlo simulations the acceleration methods were also tested using a clinical ^{99m}Tc myocardial stress/rest perfusion study acquired with the Siemens Symbia SPECT/CT scanner. Low-energy high-resolution parallel hole collimators were used, and
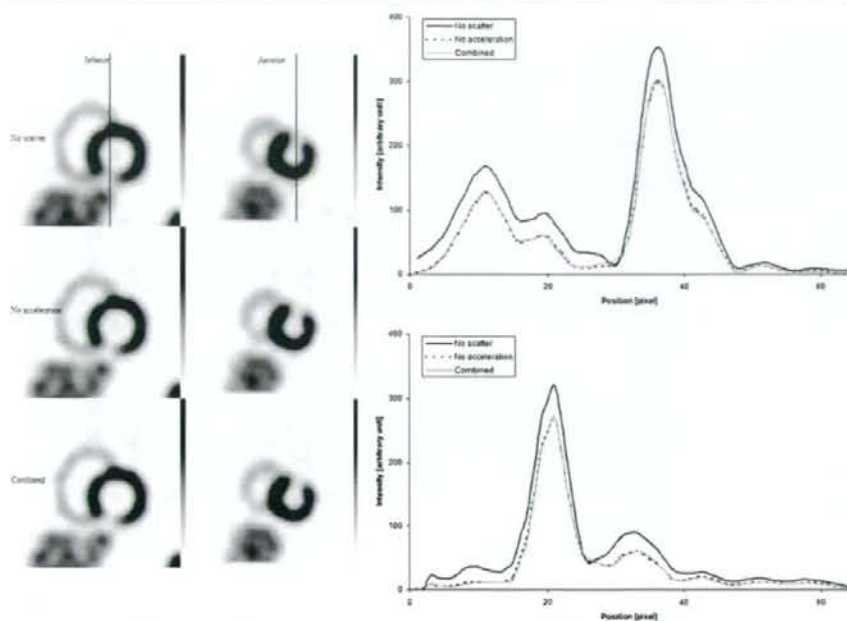
Figure 3. Short-axis slices and profiles through the heart of the MCAT phantom for reconstruction without scatter compensation (no scatter) and with MC-based scatter compensation without acceleration (no acceleration) and with coarse grid + intermittent scatter modelling (combined). Results for other acceleration methods are not shown, because they overlap the coarse grid + intermittent scatter compensation profiles. Upper profile is obtained from the image with inferior lesion and lower with anterior lesion. Locations of the profiles are shown as vertical lines.

Table 2. Lesion-to-normal myocardium and ventricle-to-normal myocardium contrasts for different MC-based scatter compensation acceleration schemes.

Scatter compensation method	Acceleration method	Contrast		
		Anterior	Inferior	Ventricle
No compensation		0.57	0.51	0.80
MC-based	No acceleration	0.64	0.58	0.91
	Coarse grid	0.65	0.59	0.93
	Intermittent	0.62	0.60	0.93
	Coarse grid+intermittent	0.64	0.59	0.93

60 projection angles over a 180° arc were acquired using a symmetric 15% energy window centred at 140 keV.

3. Results

Figure 3 shows short-axis slices and profiles through the left ventricle of the MCAT phantom for reconstruction without scatter compensation and with the MC-based scatter compensation without acceleration and with coarse grid + intermittent scatter modelling. Profiles for the